

THE FLOW OVER A ROTATING DISC-WING

Jonathan R. Potts & William J. Crowther

Fluid Mechanics Research Group, School of Engineering, University of Manchester, UK

Abstract

An experimental investigation into the aerodynamics of a rotating disc-wing has been carried out in an open-circuit wind tunnel, over a range of Reynolds number from 1.04×10^5 to 3.78×10^5 . The disc-wing considered has an axis-symmetric, approximately elliptic cross-section and hollowed out underside cavity. The spin rate was found to have only a small effect on the aerodynamic loads but shows some decrease in rolling moment. The lift and drag coefficients have been found to be independent of Reynolds number for the range of tunnel speeds tested. Observations from fluorescent paint (flow visualisation) patterns have revealed the surface flow regime. The upper surface flow is characterised by separation at a line (arc) of constant radius on the leading edge rim, followed by reattachment at a line of similar geometry. Trailing vortices detach from the trailing edge rim. The cavity flow is characterised by separation at the leading edge lip, followed by straight-line reattachment.

Nomenclature

AdvR	Advance ratio ($\Omega R_D / V$)
AR	Aspect ratio
a	Lift curve slope
a_0	Lift curve slope for a thin airfoil (2π)
C_L	Lift coefficient
C_D	Drag coefficient
C_{D0}	Profile drag coefficient
C_M	Pitching moment coefficient
C_R	Rolling moment coefficient
C_P	Pressure coefficient
k	Span efficiency factor
Re	Reynolds number
r_p	Radial position (m)
R	Disc radius (m)
D	Disc diameter (m)
T	Disc thickness (m)
V	Wind velocity (ms^{-1})
V_1, V_2	Trailing vortices
x,y,z	Roll, pitch, yaw axes
L,M,N	Rolling, pitching, yawing moments (Nm)
p,q,r	Rates of roll, pitch, yaw (rad s^{-1})
α	Geometric angle of attack
α_i	Induced angle of attack
θ	Yaw angle

τ	Finite wing factor
Ω	Spin rate (Hz)

Introduction

The rotating disc-wing, most commonly encountered as a Frisbee™ sports disc or a Discus in field athletics, offers interesting possibilities for a small, highly maneuverable unmanned air vehicle or projectile.

In its simplest form a disc-wing can be described as an axis-symmetric wing. The disc considered in this study has an approximate elliptical cross-section and hollowed out underside cavity. The centre of pressure of this configuration is ahead of the centre of the disc and hence the centre of gravity also. This results in a destabilising nose up pitching moment at typical flight angles of attack. Due to the symmetric shape of the disc, the rolling moment at this condition is approximately zero. If the disc is rotating, gyroscopic effects dictate that a pitching moment results in a precessional rolling motion of the disc. This provides pitch stabilisation at the expense of roll stability. For a typical disc rotating in the direction of positive yaw, using the conventional body fixed axes definition (Fig 1, arrows point in the positive direction and rotation), then a positive pitching moment will induce a negative roll motion.

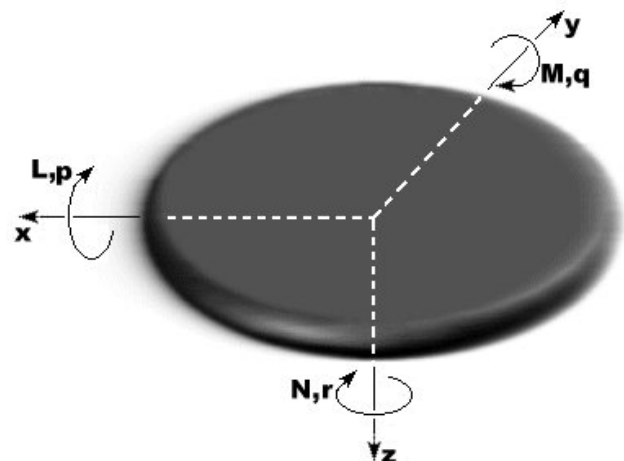


Fig 1 Schematic diagram of body fixed axes.

Well-designed disc-wings tend to have the centre of pressure close to the centre of the disc and thus show minimum tendency to roll during flight. At the other extreme, a flat plate disc with no camber and sharp leading edge

has a centre of pressure well forward of the centre of the disc leading to a rapid rolling motion in free-flight.

The U.S. Navy commissioned a project to further the development of a self-suspended flare, which was essentially a rotating disc-wing. Stilley & Carstens (1972) investigated the aerodynamics of the flare and other similar disc-wings. During that research wind tunnel test results were obtained for a non-spinning Frisbee™ model and published as typical plots of axial, normal and pitching moment coefficients. The effect of spin on the loads was investigated and found to be negligible, for the purposes of their work.

Nakamura & Fukamachi (1991) visualised the flow past a Frisbee™ using the smoke wire method. The observations are as follows: A horizontal plane of smoke filaments, aligned with the upper surface of the disc, shows a symmetric wake for the non-spinning case. A vertical smoke grid downstream of the disc shows a pair of trailing vortices formed behind the disc. The effect of spin causes an asymmetric wake.

Zdravkovich et al. (1998) studied the aerodynamics of what he called 'coin-like cylinders', which are defined as $T/D \ll 1$, where T is the thickness and D is the diameter of the cylinder. A talcum powder-paraffin film was applied to the cylinder surface to visualise the flow. With its planform parallel to the free stream, the flow over the cylinder revealed surface patterns which are similar to those observed during the present experimental work; Namely a semi-circular separation line and straight line reattachment. This gave an insight into the interaction of flow structures over the cylinder and allowed the specification of the flow topology.

This paper considers the aerodynamic forces and moments acting on a rotating disc wing and relates them to surface pressure distributions and the flow patterns inferred from surface flow visualisation. Details of the experimental methods used, together with the results are presented and discussed with reference to previous work on coin-like cylinders and disc-wings. The topology of the

flow over non-rotating discs is given based upon surface flow patterns.

Experimental Methods

The axi-symmetric geometry of the disc-wing dictates that, irrespective of the orientation of the disc to the free stream, the flow over the disc is independent of roll and yaw angle. Which means that the incidence angle is the only geometrical parameter that needs to be investigated experimentally. Therefore the flow analysis can be reduced to the testing of a disc-wing at incidence.

The Wind Tunnel The disc was tested in a low speed wind tunnel to investigate the aerodynamics over a wide range of flow speeds, incidence angles and spin rates. The open-circuit tunnel has a test section of 0.9×1.1m and a top speed of 50m/s. The forces and moments of the disc were measured using a six component overhead balance at speeds of up to 30m/s.

Apparatus Two metal frames were used to mount the discs in the wind tunnel; the first for the force/moment measurement (A), the second for the surface paint flow visualisation and the preliminary pressure measurement (B). The second metal frame (B) was necessary for surface flow visualisation; it held the disc in the horizontal plane (at 0° incidence) and limited surface drips, due to gravity, interfering with the surface flow patterns.

(A) The data rig, seen in Fig 2, was designed to vary the incidence angle and rotate the disc at

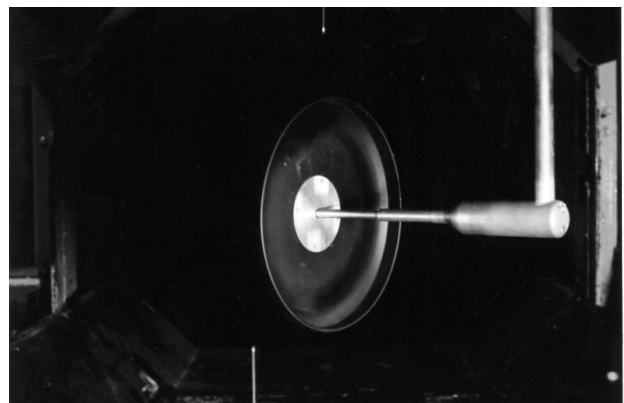


Fig 2 The data rig supporting a disc-wing, at incidence, in the wind tunnel.

different spin rates. It was essentially an L shaped arm, which consisted of a horizontal axle supported by a vertical strut. The disc, mounted with it's planform vertical, was spun on the axle so that the disc's centre of mass remained at the balance centre at all times.

(B) The flow visualisation rig was designed to manipulate incidence and spin rate. It consisted of two vertical struts connected to a horizontal crosspiece. In the centre of the horizontal bar, an axle was mounted vertically, at zero incidence, on which the disc could be spun with its planform horizontal. Incidence was adjusted using an incidence arm.

The Models The shape of the disc-wing considered in this study has a flat upper surface, an approximate elliptical cross-section and hollowed out underside cavity. The half cross-section can be seen below in Fig 3, with the axis of symmetry vertical and on the left of the figure. The diameter D is defined as the maximum chord length and the thickness T as the maximum perpendicular distance of the lip (leading edge) from the flat upper surface. The diameter is used as the characteristic length scale for this wing section which gives an aspect ratio of $4/\pi \approx 1.27$. However this quantity is constant for all disc-wings and therefore a more useful ratio to compare circular wings is T/D . For the disc in Fig 3 the ratio $T/D = 0.14$.

A number of disc-wing models were used for the testing; The first model was an aluminium disc used for the load measurement. It was turned on a lathe to the desired profile of Fig 3, and then balanced to spin true. The diameter of the disc was 0.275m and the thickness was 0.038m, $T/D = 0.14$.

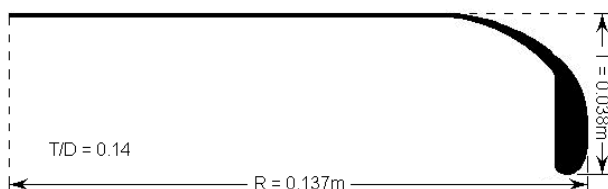


Fig 3 Cross-sectional disc-wing profile.

Two aluminium discs were used for the surface pressure measurement turned to the desired profile, see Fig 4. The surface pressures were measured on this profile as part of a preliminary

study to determine the flow characteristics. Due to requirements of this initial work, there was a 0.015m diameter hole in the centre of these two discs. One model had surface pressure tappings on the cavity surface and the other disc had tappings on the upper surface so that both surfaces of the disc could be measured. The diameter of the disc was 0.108m and the thickness was 0.014m, $T/D = 0.13$. Although these pressure measurements were taken for a disc of slightly different profile, the distributions generated from this data give evidence of similar flow structures present over both profiles. The presence of pressure tubing on the opposite side to the measuring surface will have no significant effect on the results. However, a small effect will be experienced by the tappings on the trailing edge rim of the disc.

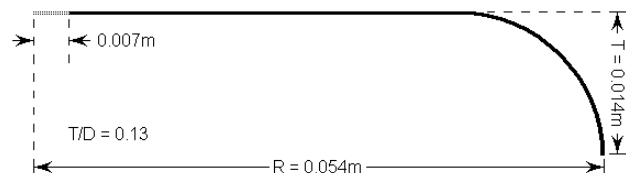


Fig 4 Cross-sectional disc-wing profile, used for pressure measurement.

Many identical discs, re-produced from a plastic injection mold, were used to visualise the surface flow. The profile, dimensions and T/D of these discs matched that of Fig 3.

Force and Moment Data The load measurement for the disc-wing was taken using the apparatus shown in Fig 2. The model was mounted on the data rig and tested over a range of Reynolds numbers from 1.13×10^5 to 3.78×10^5 , corresponding to a speed range of 6m/s to 20m/s, with incidences ranging from -10° to 30° and spin rates up to an advance ratio, ratio of disc rim speed to flow speed (AdvR), of 1. The aerodynamic forces on the disc caused the strut to deflect slightly from the centre of the balance, especially at high incidence angles. This had a significant effect on the pitch and roll moments but was compensated for by taking measurements of the moments caused by the static loading of the strut at the centre of the balance.

Interference and tare effects due to the strut were measured with the disc mounted on a

dummy support. The dummy strut was a mirror image of the measuring strut and held the disc in the correct position, on the balance centre.

Pressure Data The surface pressures on a non-rotating disc-wing were measured using a U-tube manometer connected to eight pressure tappings. Tests were performed at 14m/s ($Re = 1.04 \times 10^5$) for incidence angles 0° , 15° & 30° . These tappings were arranged in a straight line at positions 0.256R, 0.381R, 0.507R, 0.633R, 0.759R, 0.870R, 0.983R, 1.096R along the surface profile from the centre. A central pressure measurement could not be taken due to the hole in the centre of the disc. The pressure across the disc surface was measured by yawing the model at 10° increments. Since flow conditions were symmetrical, results for one half of the disc were mirrored to the other half.

The flow in the vicinity of the central hole in the disc will have an effect on the pressure distribution. However, it will later become clear, from surface flow visualisation patterns, that the same flow structures are present for a profile with or without the hole.

Surface Flow Visualisation A film of fluorescent paint, made up of a mix of two parts kerosene to one part fluorescent powder, was applied liberally to the surface of a non-spinning disc-wing. The disc was then placed in the wind tunnel and as the kerosene evaporated the time-averaged surface flow patterns were revealed. Surface paint patterns were taken for the flow over both the upper and cavity surfaces for a range of incidence angles from 0° to 30° , $Re = 2.84 \times 10^5$.

Experimental Results and Discussion

Force and Moment Data The aerodynamic forces and moments acting on the disc-wing are dependent upon speed, rotation rate and angle of attack. The loads were measured for the range of conditions that the disc-wing will experience in free flight. The present experimental results are presented in Figs 13 -15.

Referring to Fig 13 which shows the non-rotating data for $Re = 3.78 \times 10^5$. The lift curve (Fig 13a) has slope 0.05 per degree between

incidence angles 5° to 27° . Above 27° the gradient decreases as the disc approaches its stall angle and below 5° exhibits a curve. The zero lift angle is -4° . The drag curve, Fig 13b, shows a minimum, C_{D0} , of 0.08 at -4° incidence.

The pitching moment curve (Fig 13c) is non-linear and displays a negative (nose down) coefficient of -0.02 at the zero lift angle of attack (-4°). Zero pitching moment occurs at 10° incidence and provides a nose up pitching moment for higher incidence. The rolling moment (Fig 13d) is essentially zero, which is as expected for a symmetrical body.

Consider the lift and drag curves determined using finite wing theory or lifting line theory (Ref 6), see Fig 13a,b. They have been calculated using equations for a finite wing with the same aspect ratio, AR, as a disc-wing i.e. $AR = 1.27$. The lift curve is given by,

$$C_L = a(\alpha - \alpha_i) \quad (1)$$

where a is the lift curve slope,

$$a = \frac{a_0}{1 + (a_0/\pi AR)(1 + \tau)} \quad (2)$$

The previously undefined variables are, α_i the zero lift angle of attack, a_0 the lift curve slope for a thin airfoil (i.e. 2π) and τ a factor dependent upon the finite wing planform. The chosen value for α_i was taken to be -4° and a typical value for τ is 0.1. The drag curve is given by,

$$C_D = C_{D0} + \frac{k}{\pi AR} C_L^2 \quad (3)$$

where C_{D0} is the profile drag and k is the span efficiency factor. From the present experimental data $C_{D0} = 0.08$. A value of k equal to 1 was chosen. The predictions of finite wing theory (Fig 13b) give reduced lift and drag due to the viscous drag and vortex lift contributions (generated by the vortices on the surface of the disc) not accounted for by lifting line theory.

The present experimental data obtained for a non-spinning disc-wing shows good agreement with Stilley & Carstens (Ref 1,2) for a Frisbee™

with $T/D = 0.15$, as seen in Figs 13a-c. However, the present data shows a higher lift curve and the pitching moment deviates somewhat from Stilley & Carstens results. These differences are likely to be attributed to the shape of the disc they tested, it had a raised platform above the upper surface in the centre of the disc, see Fig 5.

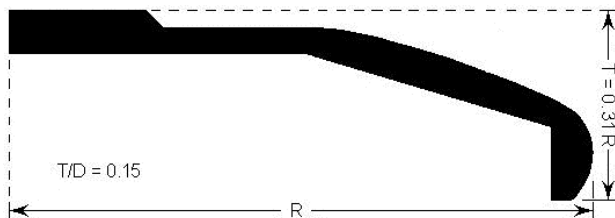


Fig 5 Cross-sectional Frisbee™ profile, Stilley and Carstens (Ref 2).

The lift and drag data presented in Fig 14, show curves for various Reynolds numbers. The curves overlay one another and are therefore independent of Reynolds number for the range of tunnel speeds tested.

The effect of spin on the lift, drag, pitching moment and rolling moment is shown in Fig 15 with curves of different advance ratios presented on each plot, for $Re = 3.78 \times 10^5$. The lift and drag curves (Figs 15a,b) are identical for AdvR 0 to 1.04, which confirms that the lift and drag are unaffected by spin. The pitching moment and rolling moment curves in Figs 15c,d follow the same general trends, for the advance ratios presented. Figs 15e,f reveal more, the pitching moment curve for AdvR 0 is greater in magnitude, for the incidence range -5° to 10° , than for non-zero advance ratios. However the maximum deviation from the AdvR 0 curve, for any given angle of attack, is 0.007. In Fig 15f, the roll trends are linear for AdvR 0 to 0.35 showing approximately zero rolling moment for all incidences. For AdvR 0.69 & 1.04 the disc has a negative rolling coefficient, for -10° to 20° incidence, which increases in magnitude for greater AdvR. This is due to the Magnus rolling moment mentioned by Stilley and Carstens (Ref 1) caused by the spin. At higher incidence, 20° , the curves are independent of advance ratio.

The free flight of a disc-wing is characterised by a 5° angle of attack at 20m/s ($Re = 3.78 \times 10^5$) and AdvR 0.35. For a disc-wing rotating in the direction of positive yaw, using the conventional body fixed axes definition, then a negative pitching moment ($C_M = -0.014$) will induce a positive roll motion, due to gyroscopic precession. This (positive yaw) spin also provides an approximately zero rolling moment ($C_R = 0.0005$).

The position of the centre of pressure of the disc is $0.145R$ at 6m/s down to $0.036R$ at 20m/s for the incidence range 0° - 10° .

Pressure Data The surface pressure distribution of the disc-wing was measured for $Re = 1.04 \times 10^5$. The data is presented as grayscale weighted contour plots for both the upper and lower (cavity) surfaces. Measurements were taken at three angles of attack, 0° , 15° & 30° (Figs 6, 16 & 17), flow direction from top to bottom.

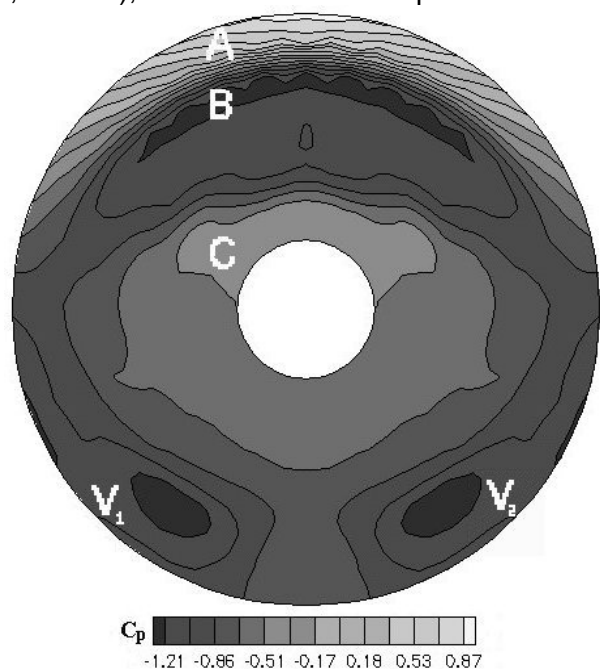


Fig 6 Upper surface pressure distribution at 0° incidence, $Re = 1.04 \times 10^5$.

The description of the upper surface pressure distribution follows with reference to Fig 6; The highest pressure region occurs on the leading edge rim (A), the rim defined as the curved section of the disc. There is a low pressure peak (B) aft of this high pressure region. The flow separates under the influence of an

adverse pressure gradient at some point between B and the high pressure region (C) just ahead of the centre. The two low pressure spots ahead on the trailing edge rim of the disc are associated with trailing vortices, which detach from the surface at V_1, V_2 .

The description of variation in the upper surface pressure distribution follows with reference to Fig 16; The pressure of the upper surface distribution can be seen to decrease, as a whole, with increased incidence. Two low pressure regions, for 15° and 30° incidence, are located on the wing-tips. Trailing vortices detach from the surface here and are lower in pressure than the positions from which the vortices detach on the trailing edge rim at 0° incidence. There is some static pressure recovery over the trailing edge part of the disc, which reaches a peak aft of the centre, for 15° & 30° incidence.

The description of variation in the cavity surface pressure distribution follows with reference to Fig 17; The pressure of the cavity surface distribution can be seen to increase, as a whole, with increased incidence. At 0° incidence the surface distribution shows a high pressure region on the trailing edge rim. The shear layer that separates off the trailing edge lip, the lip defined as the end point of the rim, is deflected into the cavity and impinges on the trailing edge rim. The leading edge rim shields much of the cavity from the free stream producing low pressure over most of the disc. For 15° & 30° incidence more of the cavity surface is exposed. At 15° the downstream half of the cavity surface is subject to high pressure. For 30° incidence the whole of the cavity is now subject to high pressure.

Surface Flow Visualisation A general description of the flow visualisation over the upper surface of the non-spinning disc, at zero angle of attack, follows with reference to Fig 7 (flow direction from top to bottom). The streak lines in the surface pattern display the time-averaged orientation of the surface streamlines; the upper surface pattern indicates that the surface flow direction is from the leading edge towards L_1 . This is indicated by the streak lines within region A. The boundary layer separates from the surface leaving a clearly visible line (L_1) and

the shear layer reattaches within region (C). The boundary layer remains attached throughout region D and then separates off the surface at L_4 . A separation bubble is formed with reversed flow (from C to B) on the surface. The reversed flow detaches from the surface (within region B) and re-circulates in the bubble. From the trailing edge, a reversed surface flow pattern is observed within region E, as fluid is drawn towards the stagnation line at L_4 . Two nodes at the points V_1, V_2 indicate where trailing vortices detach from the surface. Vorticity from the separation bubble and from beneath the cavity feeds into these vortices.

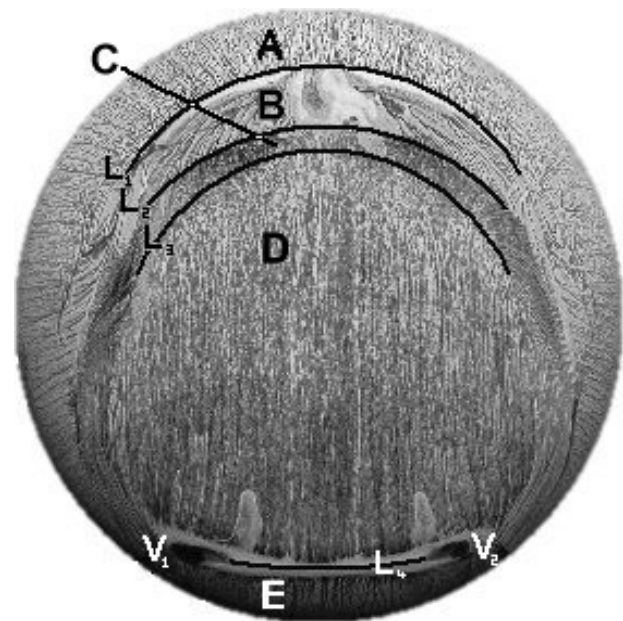


Fig 7 The upper surface paint flow visualisation pattern at 5° incidence, $Re = 2.84 \times 10^5$.

The general description of the cavity surface flow is given with reference to Fig 8 (flow direction from top to bottom); The cavity surface pattern indicates that the boundary layer separates off the leading edge lip and the shear layer reattaches to the surface leaving a straight line (L_5). The shear layer encloses a weakly circulating separation bubble (F). Aft of L_5 the boundary layer is attached throughout region G. There is a small circulating separation bubble on the inside rim of the disc (which cannot be seen on Fig 8) just ahead of the leading edge.

A description of the variation in surface paint patterns with incidence follows with reference

to Figs 7 & 18 and Figs 8 & 19. Firstly the planform coordinate system is defined; if the centre of the disc-wing is $(0, \theta)$ using polar coordinates (r_p, θ) , r_p defined as the radial position. Then the quantitative planform position of surface features, e.g. separation line, can be given. Take positive θ in the positive yaw direction ($0 \leq \theta < 2\pi$) and the point $(R, 0)$ central on the leading edge.

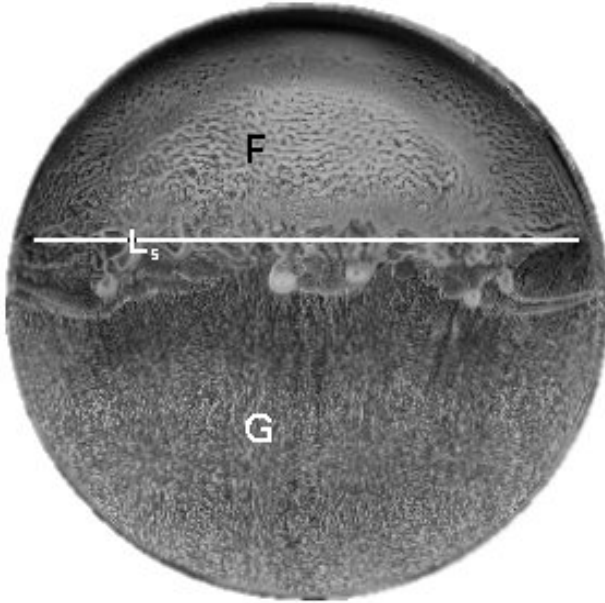


Fig 8 The cavity surface paint flow visualisation pattern at 5° incidence, $Re = 2.84 \times 10^5$.

The description of variation in upper surface patterns with incidence follows with reference to Figs 7 & 18; At 0° incidence, the flow separates at a line (arc) of constant radius, which crosses the body fixed roll axis at $(0.7R, 0)$. For increased incidence, at 5° the flow separates at the same position $(0.7R, 0)$ but then gradually moves forward to $(0.95R, 0)$ at 30°. The separa-

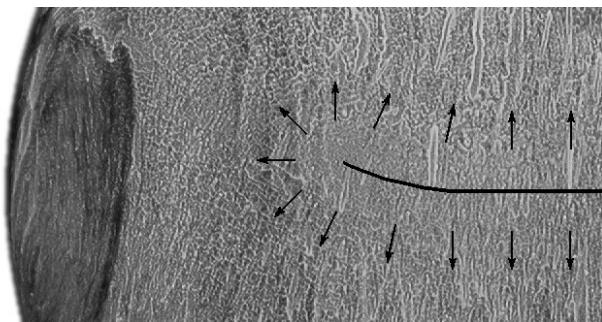


Fig 9 The time averaged stagnation line (half disc) on the upper surface paint flow visualisation pattern at 20° incidence, $Re = 2.84 \times 10^5$.

ted boundary layer can be seen to re-attach for the range 0° to 10° incidence. The surface patterns indicate that the unsteady stagnation line, of reattachment, is an arc of constant radius and moves from the position of $(0.5R, 0)$ at 0° incidence to $(0.4R, 0)$ at 10°. Fully separated flow develops between 10° and 15° incidence and the stagnation line becomes straight (perpendicular to the roll axis). This is difficult to see on Fig 18 but it is possible to see the average stagnation line for 20° incidence on Fig 9, crossing the roll axis at $(0.1R, 0)$. The arrows show the flow direction away from this stagnation line.

This stagnation line travels further downstream to a position of $(0.2R, \pi)$ at 25°, before returning upstream to a central position of $(0, \pi)$ at 30° incidence. For 25° to 30° incidence, the stagnation line narrows towards becoming a nodal point, see Fig 10 below. This radial outflow has left an uneven pattern suggesting unsteady effects as the wake dictates the surface flow in this locality.

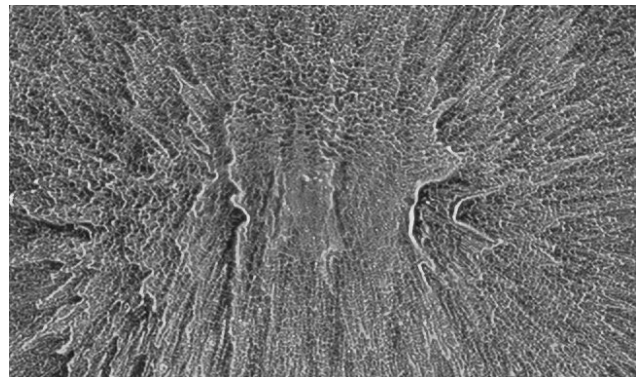


Fig 10 The stagnation line/nodal point on the upper surface paint flow visualisation pattern at 30° incidence, $Re = 2.84 \times 10^5$.

The stagnation line on the rear of the disc crosses the roll axis at position $(0.8R, \pi)$ for 0°-15° incidence. As the wake develops, through 15°, 20° incidence, the stagnation line moves position to $(0.9R, \pi)$ for the range 20°-30° incidence. The stagnation line exists between the detachment of two trailing vortices V_1, V_2 which are positioned at $(0.8R, 5\pi/6)$ and $(0.8R, 7\pi/6)$ respectively. The position of these vortices moves to $V_1(R, 2\pi/3)$, $V_2(R, 4\pi/3)$ at 20° incidence and $V_1(R, \pi/2)$, $V_2(R, 3\pi/2)$ for 25°-30°.

The description of variation in cavity surface patterns with incidence follows with reference to Figs 8-19; At 0° incidence, the shear layer, separates off the leading edge, reattaches to the surface producing a line (arc) of constant radius, which crosses the body fixed roll axis at (0.6R,0). For increased incidence this reattachment line becomes straight and perpendicular to the roll axis, at 5°-10° the flow reattaches at (0.2R,0). For 15°-20° the flow reattaches at (0.5R,0) and 25°-30° at (0.6R,0). Weak re-circulation occurs ahead of the reattachment line for 0°-25° incidence behind the leading edge rim. This re-circulation has not disturbed the surface paint much, observations of the paint patterns show reversed surface flow but the flow here would be better described as stagnant. At some angle between 25°-30° the stagnant air bubble shielded by the leading edge lip breaks down and upstream of the stagnation line, for 30° incidence, the paint patterns show that the reversed surface flow can no longer be described as stagnant. There are two foci of attachment for 0° incidence. These are located at $(0.6R, \pi/5)$ and $(0.6R, 9\pi/5)$. There is a small re-circulation bubble, which was found inside the trailing edge rim, for 0°-10° incidence. The bubble breaks down for higher incidence and the cavity surface flow is attached to the trailing rim before it separates at the trailing edge lip. It is also worth noting that, on the downstream half of the cavity, the streak lines aft of the reattachment can be seen to converge on the centre (roll axis) line, particularly for higher incidence. This is due to the convergence of fluid as the rim narrows towards the trailing edge.

Zdravkovich et al. (Ref 4) describes the separation from the semi-circular sharp edges of coin-like cylinders and straight-line reattachment, at zero incidence. For the disc-wing considered in the present study, also at zero incidence; the initial separation and subsequent reattachment lines on the upper surface were both observed to be semi-circular. However, the reattachment on the cavity surface was observed to be a straight line for 5° incidence. The flow structures observed over both bodies are very similar.

Proposed Disc-wing Flow Topology The proposed topology of the flow over non-rotating discs is given based upon surface flow

patterns. The two-dimensional flow cross-section shown in Fig 11 depicts many of the flow structures that have been previously discussed. In addition, the small separation bubble can be seen on the inside of the cavity rim with stagnation point on the trailing edge lip. From this stagnation point on the trailing edge lip, the surface flow was drawn up the back of the trailing edge rim, towards another stagnation point at the top of the rim. This was seen as reversed flow on the upper surface patterns. The turbulent wake was proposed based on the smoke wire flow visualisation carried out by Nakamura & Fukamachi. The wake shown in Fig 11 has a downwash angle more like that observed downstream of a rotating disc (Ref 3).

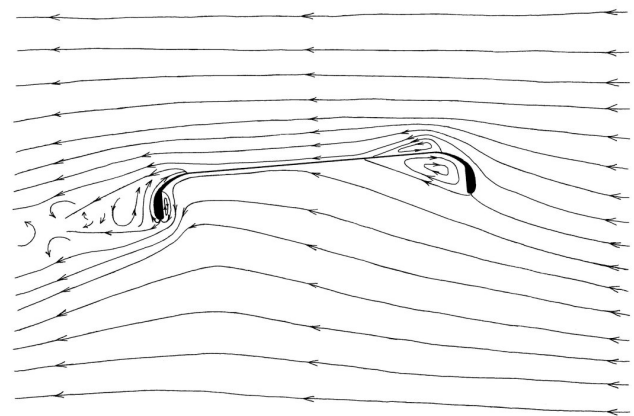


Fig 11 2D cross-sectional flow topology for a non-rotating disc-wing, 5° incidence.

The three-dimensional flow topology shown in Fig 12 depicts many of the flow structures previously described with reference to Fig 7. In addition, radial inflow occurs on the rim surface almost all the way around the circumference. There is reversed flow within the separation bubble towards a central node of separation.



Fig 12 3D flow topology and upper surface pattern for a non-rotating disc-wing at 5° incidence, $Re = 2.84 \times 10^5$.

The trailing vortex filaments (Fig 12) move closer to each other downstream of the disc with vorticity in the direction shown, again with reference to the observations of Nakamura & Fukamachi (Ref 3).

Conclusions

The basic load characteristics of a non-rotating disc-wing with angle of attack are in reasonable agreement with finite wing theory and the U.S. Navy wind tunnel tests for a similar shaped disc.

For the tested disc-wing model, the zero lift angle of attack is -4° and the corresponding zero lift pitching moment is -0.0465 Nm .

Spin has a relatively small effect on the aerodynamic forces and moments. For a typical 5° flight angle of attack, at $Re = 3.78 \times 10^5$ and $AdvR = 1$, the lift coefficient is increased by 0.0322 (6.4%), the drag coefficient is decreased by 0.0061 (3.9%) and the pitching moment coefficient is increased by 0.0067, rolling moment is increased by 0.0100, from the corresponding values at $AdvR = 0$.

The lift and drag coefficients have been found to be independent of Reynolds number for the range of tunnel speeds tested.

The flow over the upper surface of the disc is characterised by separation on the leading edge rim at a position of $(0.7R, 0)$. This is followed by reattachment at around $(0.5R, 0)$. The flow then separates at around $(0.8R, \pi)$ before the trailing edge. Trailing vortices detach from the upper surface at two symmetrical positions $V_1(0.8R, 5\pi/6)$, $V_2(0.8R, 7\pi/6)$.

The cavity flow is characterised by separation at the leading edge lip, followed by attachment (in a straight-line perpendicular to the free stream) at $(0.2R, 0)$ ahead of the centre, then separation ahead of the trailing edge.

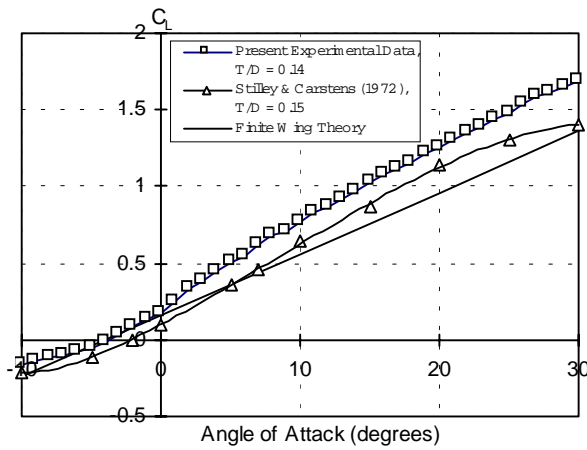
Acknowledgements

The authors would like to acknowledge the experimental work of M. Stone and C. Martin-Henry, students at the University of Manchester. We would like to thank D. Mould at the

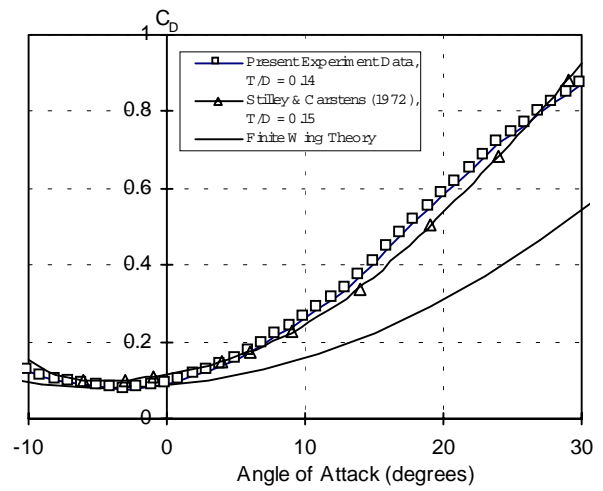
Goldstein Laboratory for the skilled construction of the rig and disc. This research was funded by the EPSRC, award reference number 98317373.

References

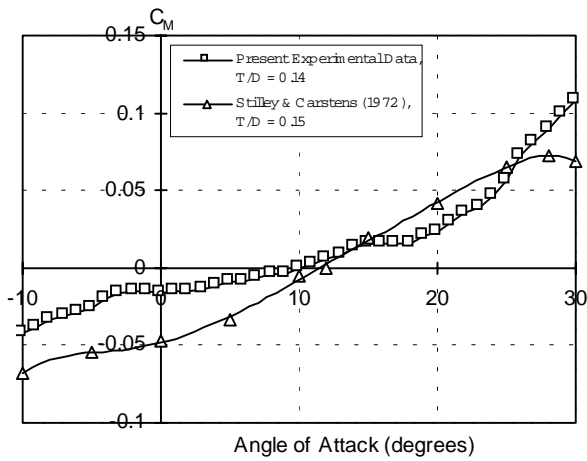
- 1 Stilley G.D. & Carstens D.L., Adaptation of Frisbee Flight Principle to Delivery of Special Ordnance, AIAA Paper No. 72-982, 1972.
- 2 Stilley G.D., Aerodynamic Analysis of the Self-Suspended Flare, Honeywell Inc., NAD/Crane RDTR No.199, AD740117, 23 Feb. 1972.
- 3 Nakamura Y. & Fukamachi N., Visualisation of Flow Past a Frisbee, Fluid Dyn. Res., v7, pp31-35, 1991.
- 4 Zdravkovich M.M., Flaherty A.J., Pahle M.G. & Skelhorne I.A., Some Aerodynamic Aspects of Coin-like Cylinders, JFM, v360, pp73-84, 1998.
- 5 Tobak M. & Peake D.J., Topology of Three Dimensional Separated Flows, Ann. Rev. Fluid Mech., v14, pp61-85, 1982.
- 6 Anderson, Jr. J.D., Fundamentals of Aerodynamics (2nd Ed.), McGraw-Hill Inc., pp340-343, 1991.



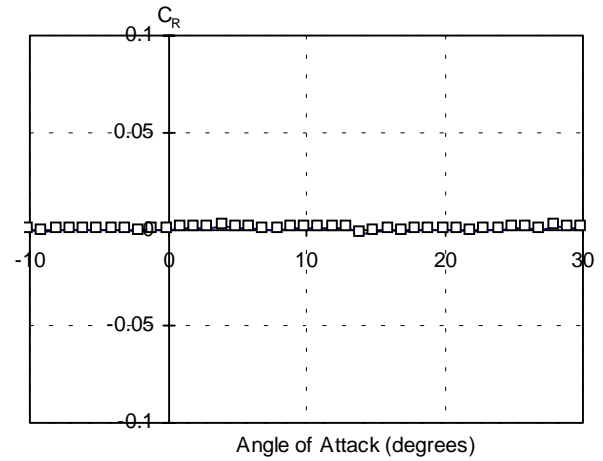
(a) Lift coefficient.



(b) Drag coefficient.



(c) Pitching moment coefficient.



(d) Rolling moment coefficient.

Fig 13 Force and moment characteristics at zero spin rate, $Re = 3.78 \times 10^5$.

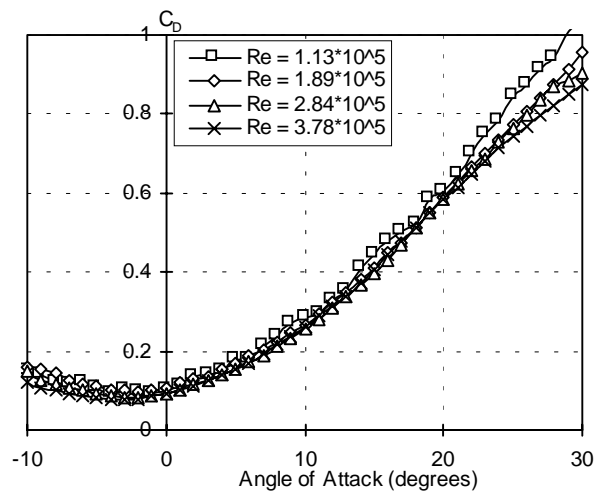
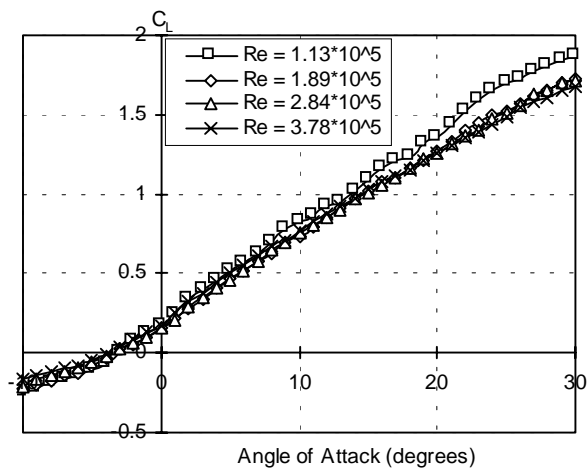
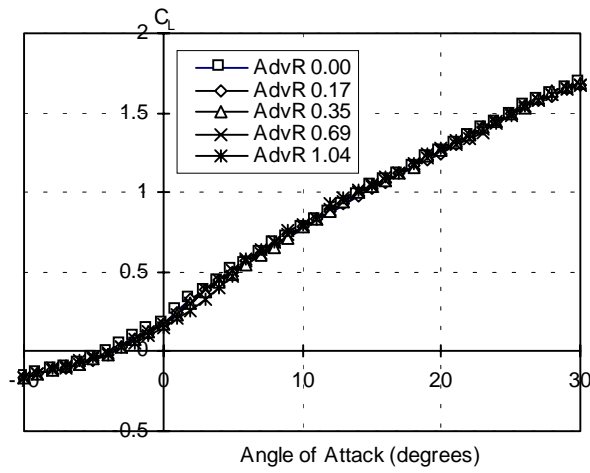
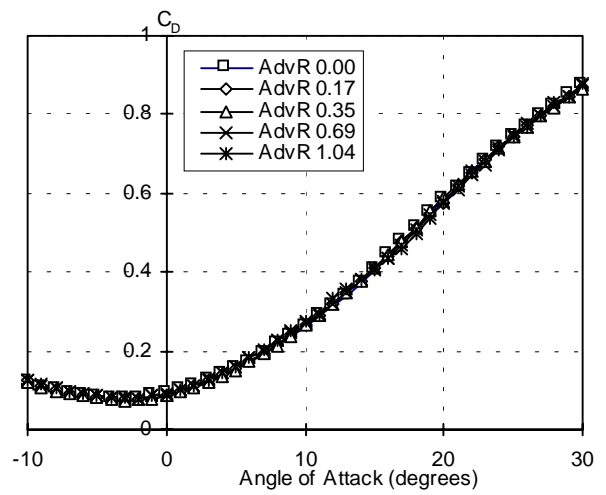


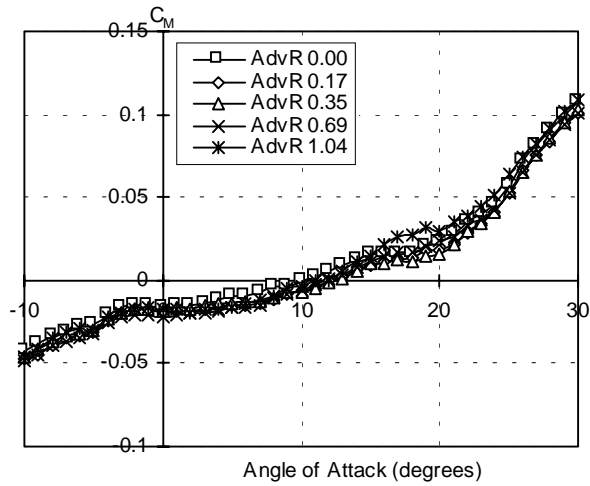
Fig 14 Effect of Reynolds number on lift and drag coefficients. Tunnel speed varied to achieve different Re (6, 10, 15, 20m/s).



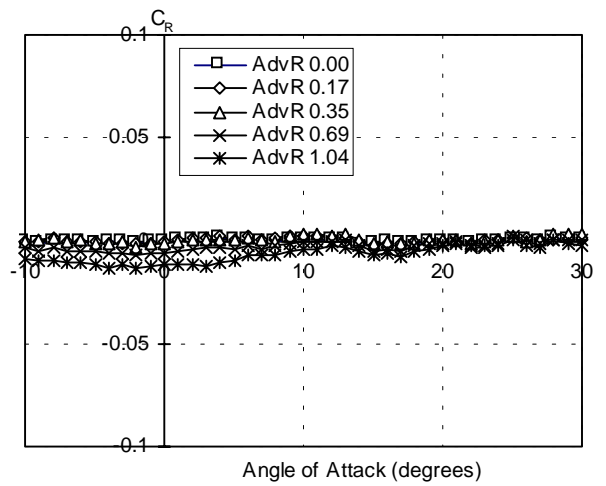
(a) Lift coefficient.



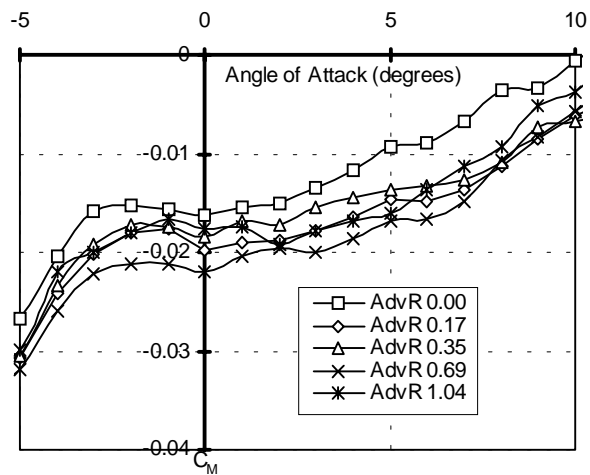
(b) Drag coefficient.



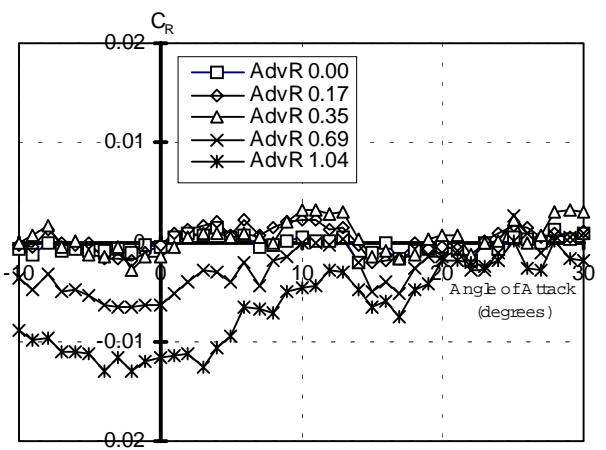
(c) Pitching moment coefficient.



(d) Rolling moment coefficient.

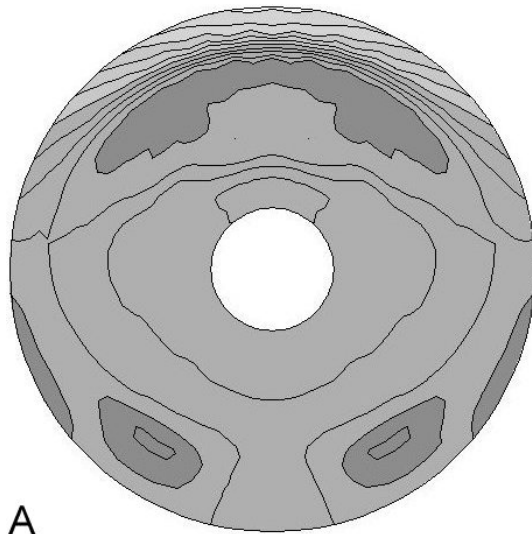


(e) Pitching moment coefficient (detail).

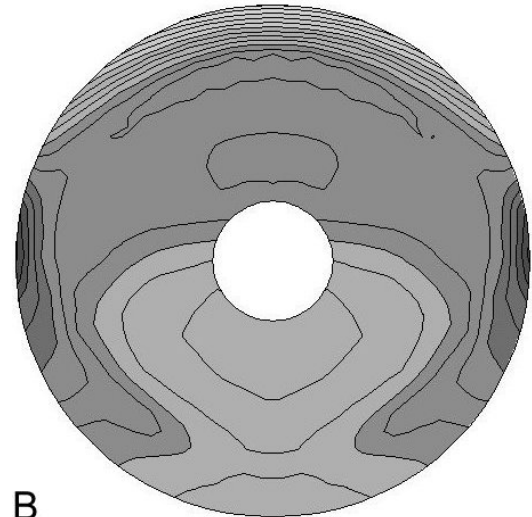


(f) Rolling moment coefficient (detail).

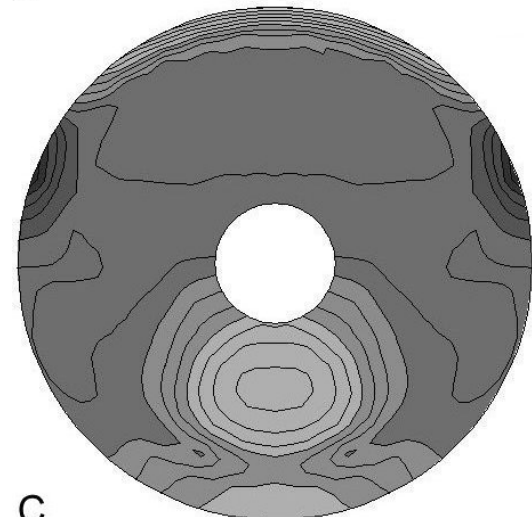
Fig 15 Force and moment characteristics for various advance ratios, $Re = 3.78 \times 10^5$.



A



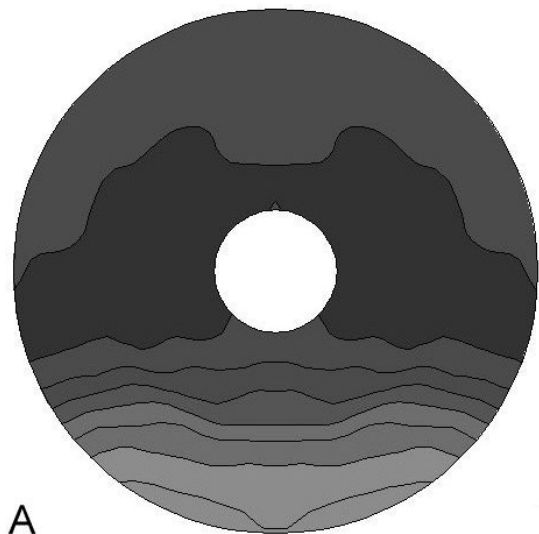
B



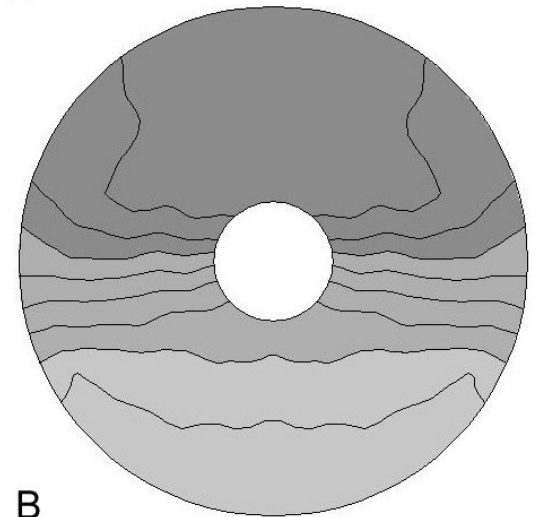
C



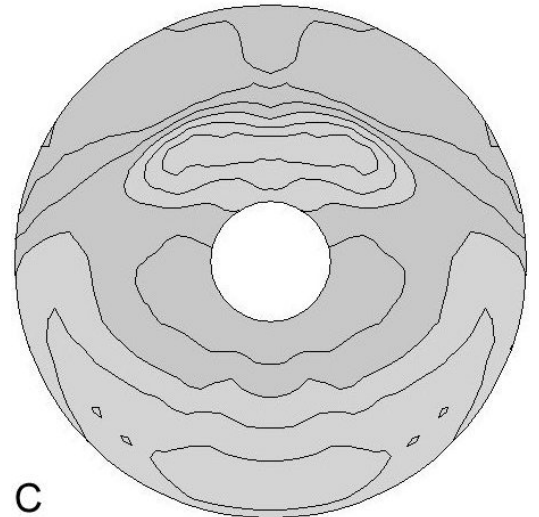
Fig 16 Upper Surface Pressure Distribution at incidence angles (A) 0° (B) 15° (C) 30°, for $Re = 1.04 \times 10^5$.



A



B



C



Fig 17 Cavity Surface Pressure Distribution at incidence angles (A) 0° (B) 15° (C) 30°, for $Re = 1.04 \times 10^5$.

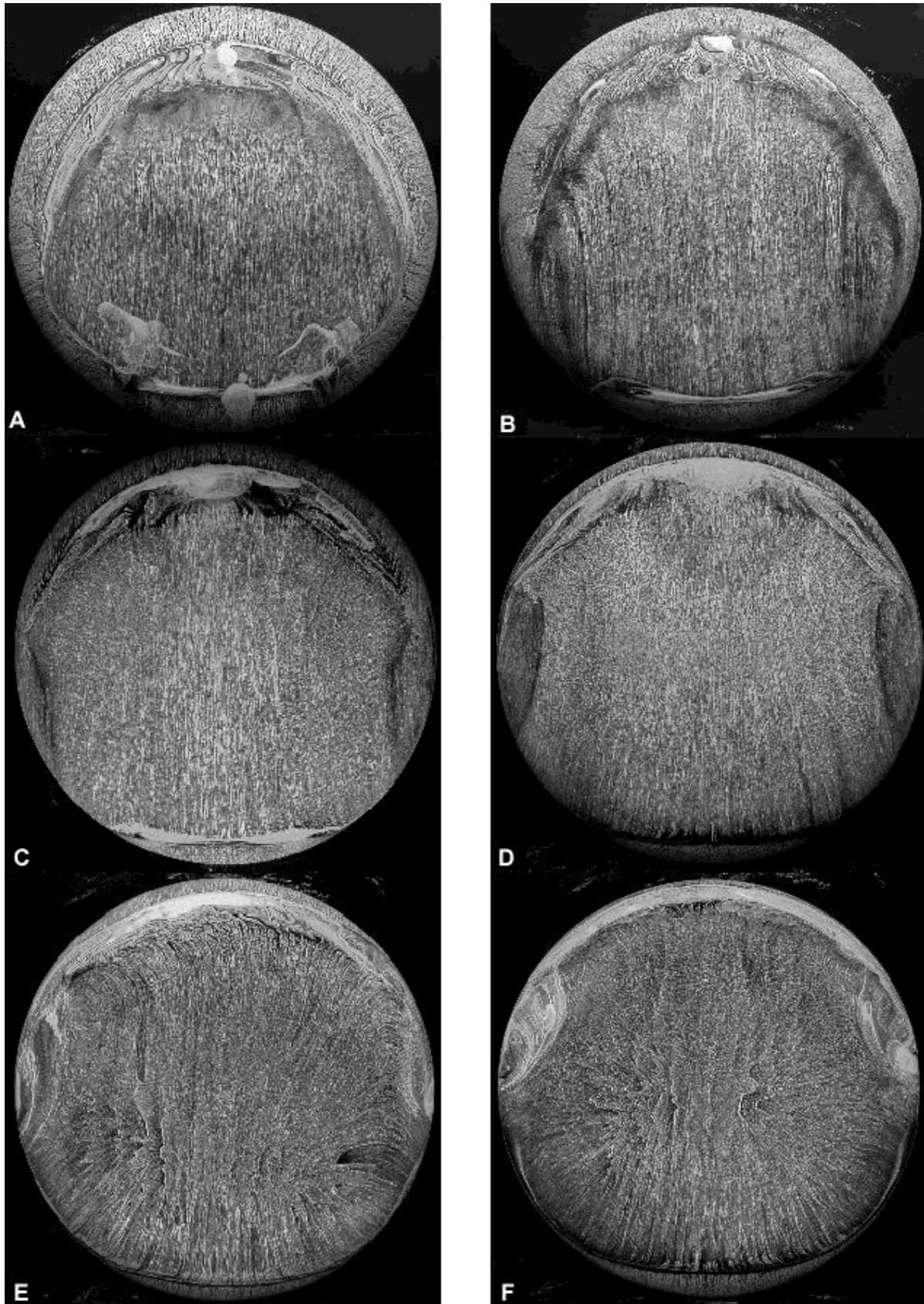


Fig 18 Upper surface paint flow visualisation patterns at incidence angles (A) 0° (B) 10° (C) 15° (D) 20° (E) 25° (F) 30°, for $Re = 2.84 \times 10^5$.

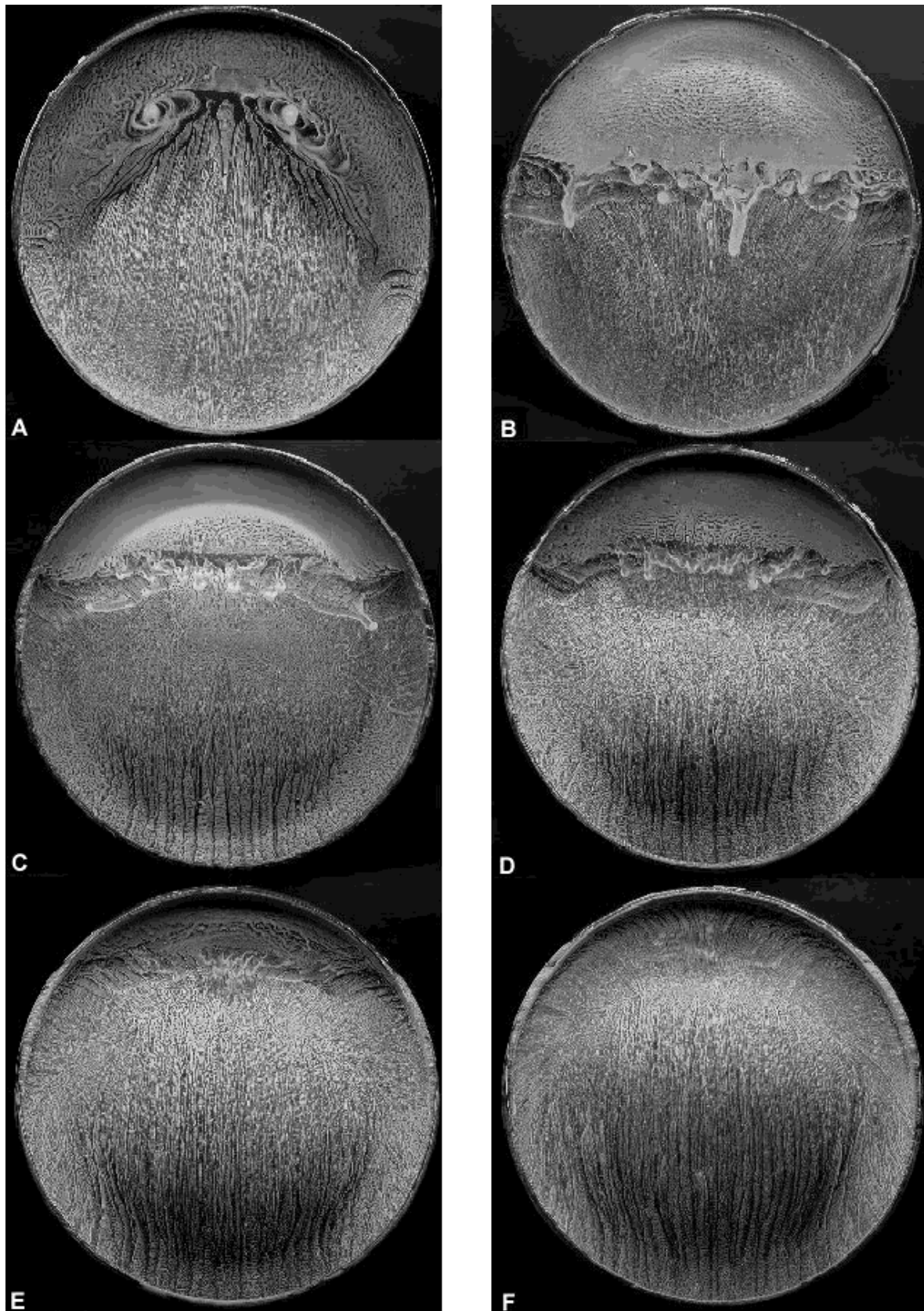


Fig 19 Cavity surface paint flow visualisation patterns at incidence angles (A) 0° (B) 10° (C) 15° (D) 20° (E) 25° (F) 30°, for $Re = 2.84 \times 10^5$.